Journal of Computational Physics 402 (2020) 108896

Contents lists available at ScienceDirect

Journal of Computational Physics

www.elsevier.com/locate/jcp

Higher-order simulation of two-phase compositional flow in 3D with non-planar fractures

Ali Zidane, Abbas Firoozabadi *

Reservoir Engineering Research Institute, Palo Alto, CA, USA

ARTICLE INFO

Article history:
Received 31 January 2019
Received in revised form 11 August 2019
Accepted 13 August 2019
Available online 20 August 2019

Keywords:
Multiphase flow
Fractured reservoirs
Higher-order methods
Non-planar fractures
Unstructured gridding

ABSTRACT

Non-planar fractures are often created in hydraulic fracturing. These irregular shape fractures may reduce the penetration into the formation; they may also improve the reservoir reach. Accurate flow simulation of two-phase compositional flows in domains with complex non-planar fractures is beyond the capabilities of current numerical models. In this work we present a higher-order numerical model for compositional two-phase flow in a domain with non-planar fractures. Fully unstructured gridding in 3D is a natural choice for description of geometry with irregular fracture shapes. We apply the concept of fracture cross-flow equilibrium (FCFE) in simulations of porous media flows with non-planar fractures. FCFE allows accurate flow and composition calculations at low CPU cost. Our implementation is in the context of the hybridized form of the mass conservative mixed finite element (MFE) and the higher-order discontinuous Galerkin (DG) method. In this work we introduce a simple and effective approach for design of non-planar fractures through the mesh interface that connects computer-aided-design (CAD) software to the mesh generator. In our algorithm we can simulate all ranges of fracture permeability accurately as opposed to other approaches where low permeability fractures affect the accuracy.

Introduction

Exploitation of unconventional hydrocarbon resources including shale and tight sand formations depends on fracking. The hydraulic fractures improve the well productivity in tight formations and provide economic production rates [38].

Fracture stimulation in tight formations produces a complex facture network [21,32]. The complexity of fracture networks is influenced by subsurface geomechanics, in particular the in-situ stress, and the fracturing fluid [32,44]. By advanced technologies such as microseismic monitoring, strain sensing and fiber optics, it has been shown that fractures grow and develop in different ways [28,19].

Some authors have argued that most hydraulic fractures tend to have non-planar geometries [23,9,39,24,34,8,36,37]. Non-planar fractures cannot be described in a flat plane in 3D. At elevated in-situ stresses, fractures grow in planar surfaces. However, at low in-situ stresses fractures may grow apart and non-planar fractures may develop when the distance between fractures reduces [24]. When the wellbore is aligned with the plane of the preferred fracture direction, a planar fracture propagates parallel to the maximum horizontal compressive stress. On the other hand, when the wellbore is not aligned with the principal stress plane, the fracture will tend to become perpendicular to the minimum horizontal stress since this

* Corresponding author.
E-mail address: af@rerinst.org (A. Firoozabadi).

https://doi.org/10.1016/j.jcp.2019.108896
0021-9991/

requires the least energy for fracture propagation; the result is a non-planar propagation path and S-shaped propagation trajectories [23]. Fracture configurations according to recent laboratory experiments [45] can be divided into three different categories, single flat fractures, multiple-parallel fractures, and spiral shape fractures.

Experiments in the laboratory on fracturing are the main method to investigate fracture initiation and propagation. Zhou et al. [47,48] studied the fracture propagation using supercritical CO_2. Li et al. [16] studied the effect of different fracturing fluids on fracture formation. Van de Ketterij and Pater [29] studied the effect of different perforation angles on fracture initiation at a well deviation of 45°. Ispas et al. [15] studied the effect of different deviation angles on fracture propagation but neglected the perforation angles. Later, the effects of different deviation and perforation angles on fracture geometry was investigated by Zhu et al. [50]. Weng [35] examined the turning and twisting shapes of non-planar fractures. In recent laboratory experiments by Zhang [45] fracture propagation was investigated in tight formations under different horizontal stress conditions. The three main fracture configurations discussed above were observed. The non-planar spiral shape fracture was created at high perforation density. Different studies have revealed a close relationship between perforation parameters and fracture geometry [31,29].

In addition to laboratory observations of non-planar fracture propagation and shape, different numerical studies have been conducted on the subject. Olson [23] proposed a 2D model to analyze non-planar fracture propagation under different boundary conditions. Xu and Wong [38] presented a 3D simulator that describes non-planar fracture growth. Zhang et al. [46] studied, by means of microflow simulation, the effect of fracture roughness on the relationship between hydraulic and mechanical apertures.

The finite element method (FEM) has been adapted as the main methodology in describing fracture propagation [30,59]. Different authors have considered the modeling of fracture propagation using the FEM [5,22,7]; however, to account for fluid flow in fractures, these methods require computationally expensive remeshing techniques to simulate the fracture growth [25]. Finite element meshes require consistent mesh adaptation to capture the fracture geometry in simulation of hydraulic fracturing which increases significantly the simulation cost.

The limitation of the traditional FEM relates to the high computational cost. The cost arises from the need to match the fractures to the matrix elements. To account for fracture complexity efficiently, the generalized finite element method (GFEM) and the extended finite element method (XFEM) were introduced [11,2,18]. The idea of both methods is to remove the physical connection between the fractures and the matrix to alleviate the need for remeshing.

Unlike simulation of fracture initiation and propagation, simulation of fluid flow and species transport in fractured media containing hydraulic fractures are covered in a limited number of papers. Zhou et al. [49] presented a semi-analytical method for production forecast from unconventional reservoirs. The semi-analytical method consists of integrating the unsteady pressure equation to obtain a semi-analytical spatial and temporal expression for the pressure. The approach can be employed to forecast production in unconventional formations in single-phase compressible flow. Cipolla et al. [6] proposed a model for hydrocarbon production forecast from unconventional resources with complex fractures. The simulation is based on the unstructured Voronoi grids. This approach imposes a severe restriction on the size of time step due to the fine refinement to capture the geometry/shape of the fractures. The model is limited to 2.5D (2.5D refers to pillar type of grids as prisms, hexahedra or Voronoi grids) fracture representation. Simulation of twisted fractures may not be feasible by this approach. The high computational cost of this type of unstructured grids has motivated various authors to propose alternatives. Filho and Sepehrnoori [9] have used the embedded discrete fracture model (EDFM) to simulate compositional two-phase flow in hydraulic fractures. The authors justified the use of Cartesian grids in their work because they believed the computational cost is high in unstructured grids in the discrete fracture representation. As we will demonstrate in this work, a fully unstructured gridding in 3D is the method of choice to model non-planar fractures efficiently without the need of grid refinement. The EDFM may overcome the computational limitations of unstructured Voronoi grids. However, because the fractures are embedded in a Cartesian grid types, the method may not be used for non-planar fractures with realistic twisted shapes. The EDFM representation may only be effective in simple non-planar fracture shapes. Embedding a twisted fracture shape in a preexisting domain grids require either non-prismatic type of matrix elements or extreme refinements in Cartesian grids to match the fracture meanders, which makes the simulation cost very high.

In this work we present an algorithm based on fully unstructured grids to simulate compositional two-phase flow with complex non-planar fractures. We apply the powerful concept of fracture cross-flow equilibrium (FCFE) [12,51,53] to simulate flow and species transport in non-planar fractures in 3D unstructured gridding. To avoid the high-computational cost of explicit time scheme in small fracture elements due to the Courant-Freidrich-Levy (CFL) condition we use our implicit model for compositional two-phase flow [52] in the fractures. The FCFE approach allows the use of large grids near the fractures. The total number of grids is therefore reduced compared to the approaches which are based on Voronoi grid types. Avoiding the CFL restriction and eliminating the need for small elements adjacent to the fractures reduce computational cost drastically.

The rest of the paper is organized as the following. In the next section we provide a description of the CAD interface followed by the differential equations that describe the flow and a brief overview of the numerical discretization. Five numerical examples are presented to demonstrate the efficiency, accuracy and ease of integrating complex non-planar fractures in the matrix domain.

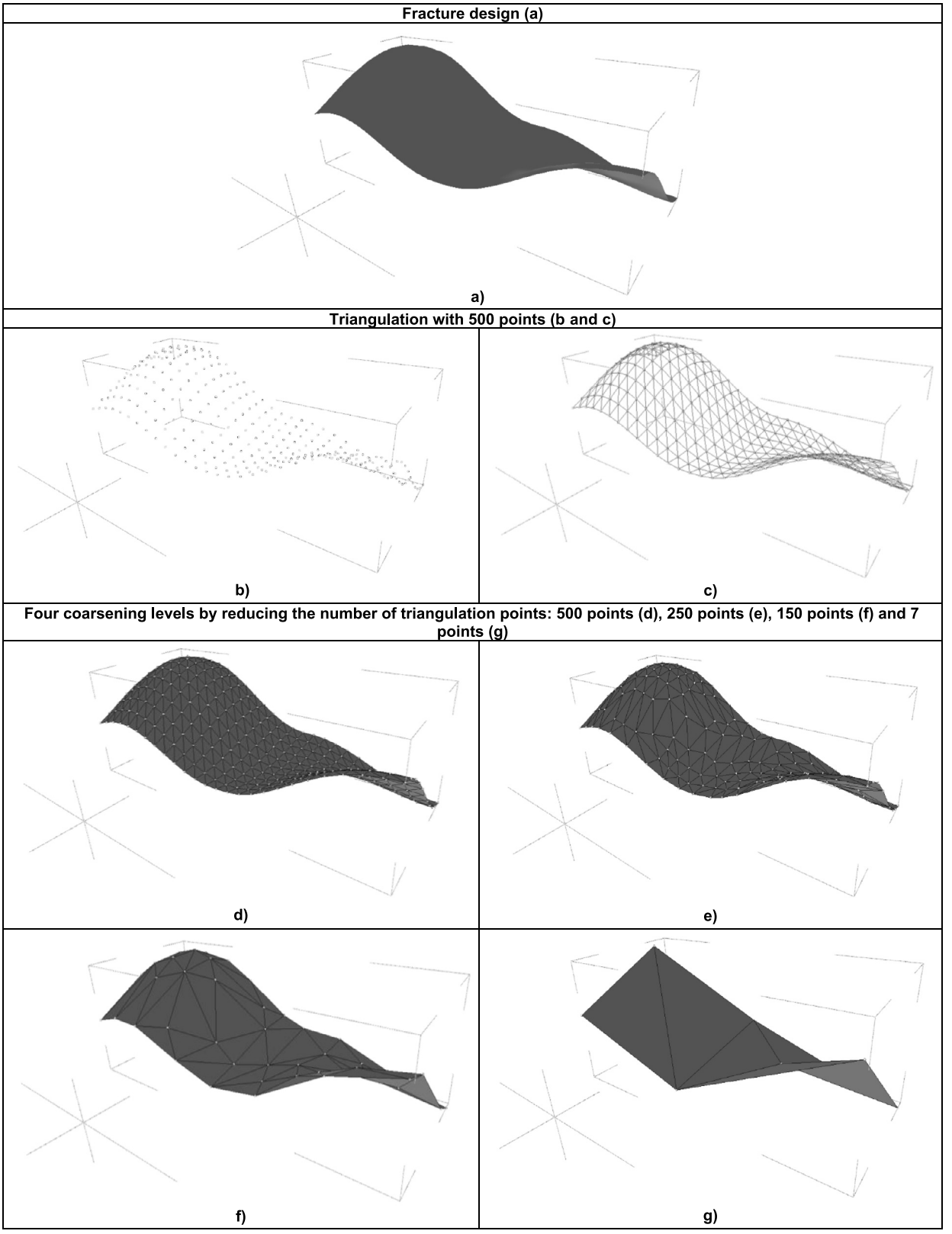

Fig. 1. Non-planar fracture design and mesh.

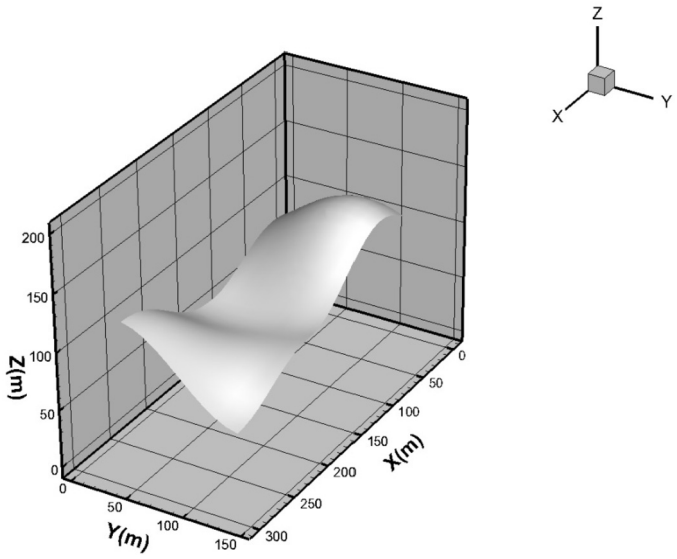

Fig. 2. Domain and fracture: Example 1.

Table 1
Relevant data: Example 1.

Parameter	Value
Matrix permeability [md]	10
Fracture permeability [md]	10^5
Porosity [%]	20
Fracture thickness [mm]	2
Temperature [K]	311
Pressure [bar]	69
Injection rate [pv/year]	0.1

CAD interface

Our algorithm includes an interface to the computer-aided-design (CAD) software, and tetgen [27] for generation of the unstructured tetrahedrons. The interface allows to design and generate a complicated domain and non-planar fracture shapes. The fracture shape is designed in 3D using the tools and features available in the CAD software (Fig. 1a).

In our interface we generate a set of points to describe the 3D fracture shape (Fig. 1b). The density of the points depends on the complexity of the fracture shape, and the importance of capturing the complexity in a given simulation. The generated set of points are then triangulated to match the faces of unstructured tetrahedrons of the matrix domain (Fig. 1c). Tetrahedrons are generated in a way to honor the location of the fractures. The triangulation of tetrahedrons starts at the fracture (triangular) elements and then to the rest of the matrix domain. Therefore, the matrix elements are smaller near the fractures and are large away from the fractures. Fractures are represented by the interfaces of the matrix elements; each fracture element has 2 adjacent matrix elements, unless the fracture is at the boundary of the domain. In this case it has one matrix connection.

In our algorithm one could choose to coarsen or refine the fracture elements by keeping the total number of matrix elements within the same range. The fracture triangular 2D elements should match the interfaces of the 3D matrix elements. Note that the fractures are represented by $(n-1)$-D elements in n-D domains. Figs. 1(d-g) show 4 different levels of mesh coarsening in the fracture (500 points, 250 points, 150 points and 7 points). The fracture shape is affected by the coarsening process; however, depending on the accuracy required, in our interface one can readily adjust the fracture mesh.

Governing equations

For the sake of completeness, we present briefly the main equations that govern the compositional two-phase flow in fractured media. Equations in the matrix domain and the fractures are treated separately.

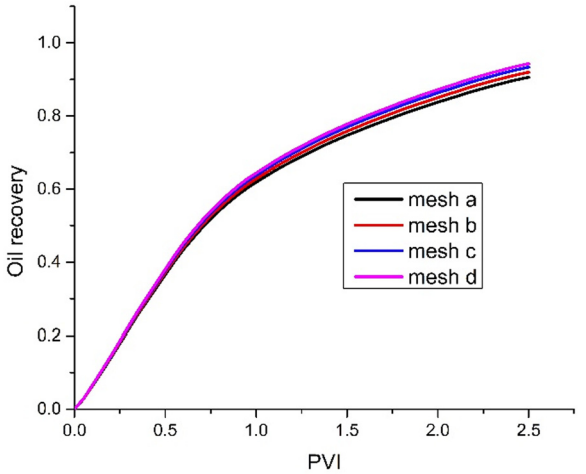

Fig. 3. Oil recovery in different mesh refinements (mesh a: 2500, mesh b: 5000, mesh c: 10,000, mesh d: 20,000): Example 1. (For interpretation of the colors in the figure(s), the reader is referred to the web version of this article.)

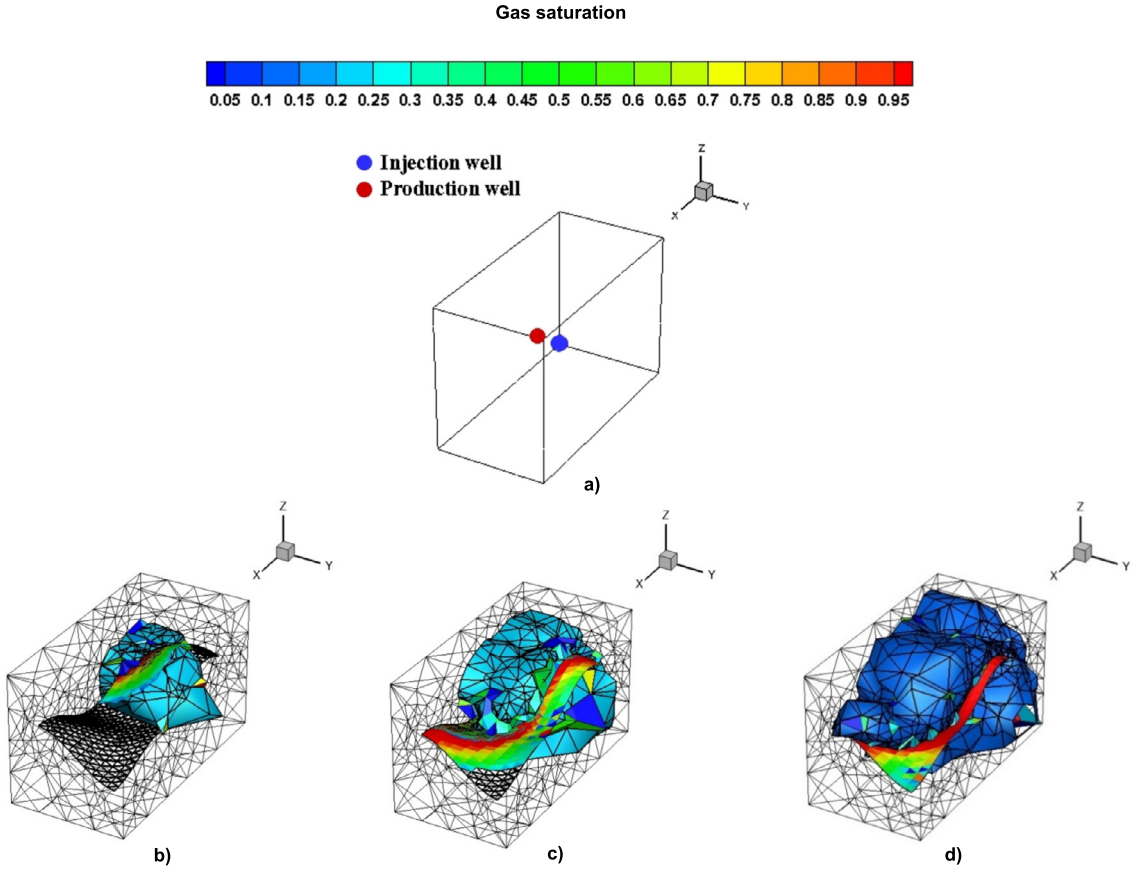

Fig. 4. Location of injection and production wells, fracture removed to show location of the wells (a); Gas saturation at 10% (b), 20% (c) and 50% (d) PVI with 10,000 element mesh: Example 1.

Matrix domain

The mass transport equations for a component i in an n_c-component mixture in two-phase are given by:

$$\phi \frac{\partial c z_i}{\partial t} + \nabla . \left(\sum_{\alpha} c_{\alpha} x_{i,\alpha} \boldsymbol{v}_{\alpha} \right) = F_i, \quad i = 1 ... n_c \text{ in } \Omega \times (0, \tau) \tag{1}$$

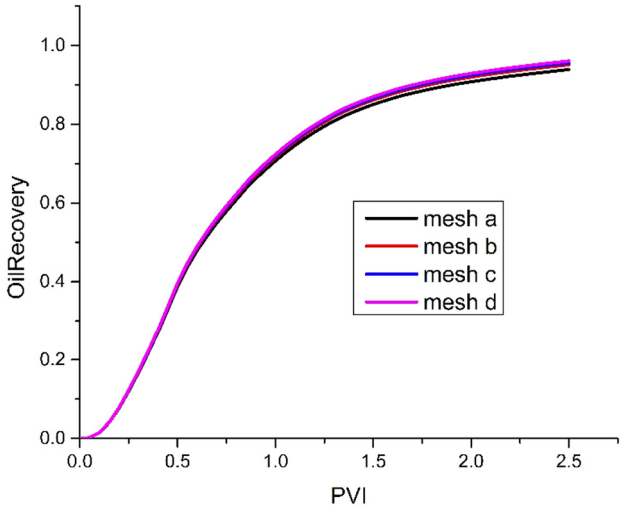

Fig. 5. Oil recovery in different mesh refinement (mesh a: 2500, mesh b: 5000, mesh c: 10,000, mesh d: 20,000): Example 2.

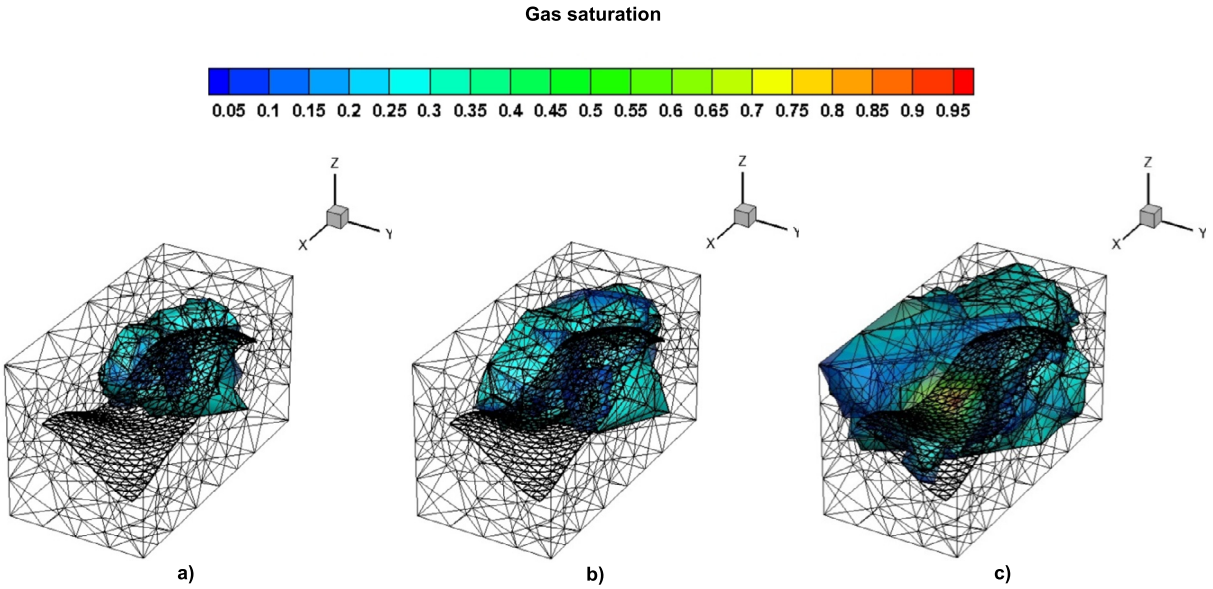

Fig. 6. Gas saturation at 10% (a), 20% (b) and 50% (c) PVI with 10,000 element mesh; injection well located at the origin and production at the top diagonally opposite corner: Example 2.

and

$$\sum_{i=1}^{n_c} z_i = \sum_{i=1}^{n_c} x_{i,\alpha} = 1 \tag{2}$$

where ϕ denotes the porosity, $\boldsymbol{v}_\alpha$ the velocity of phase α, c the overall molar density of the mixture; z_i and F_i are the overall mole fraction and the sink/source term of component i in the mixture, respectively. c_α is the molar density of phase α and $x_{i,\alpha}$ is the mole fraction of component i in phase α. Ω is the computational domain and τ denotes the simulation time and n_c is the number of components.

The velocity of phase α is given by Darcy's law:

$$\boldsymbol{v}_\alpha = -\frac{\mathbf{K}k_{r\alpha}}{\mu_\alpha}(\nabla p - \rho_\alpha \mathbf{g}) = -\lambda_\alpha \mathbf{K}(\nabla p - \rho_\alpha \mathbf{g}), \quad \alpha = o, g \tag{3}$$

where $\mathbf{K}$ is the absolute permeability tensor, $k_{r\alpha}$, μ_α and ρ_α are the relative permeability, dynamic viscosity and mass density of phase α respectively, with $\lambda_\alpha = k_{r\alpha}/\mu_\alpha$; p is the pressure and $\mathbf{g}$ is the gravitational acceleration. We use the method in [17] to describe the phase viscosities.

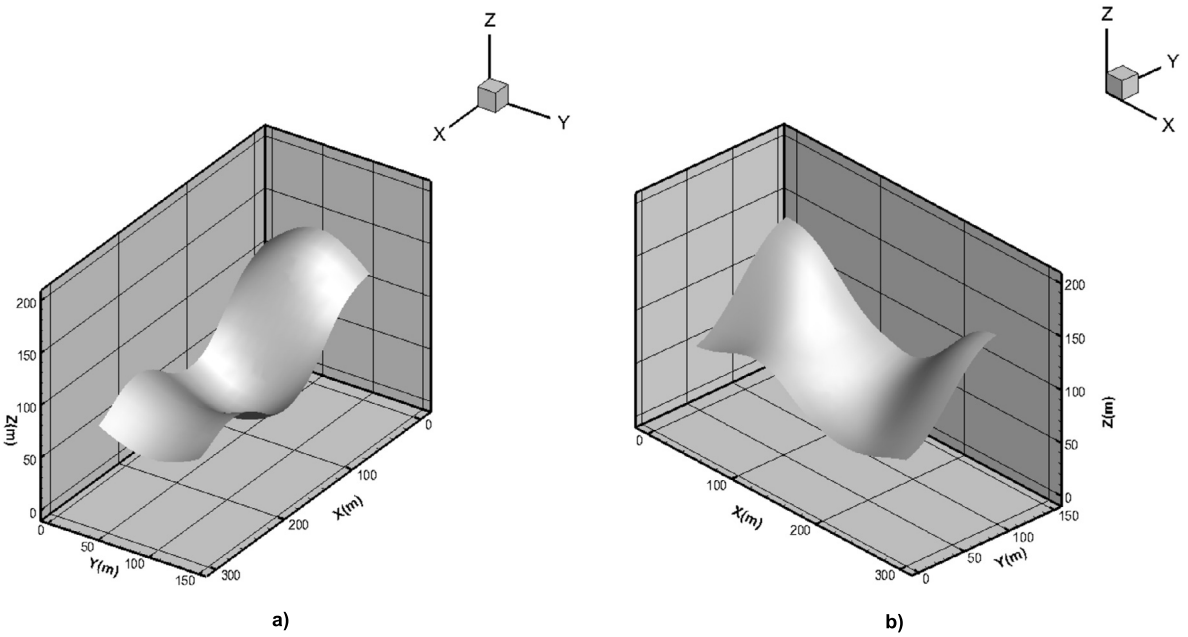

Fig. 7. Different fracture shapes used for similar problems as in Examples 1 and 2.

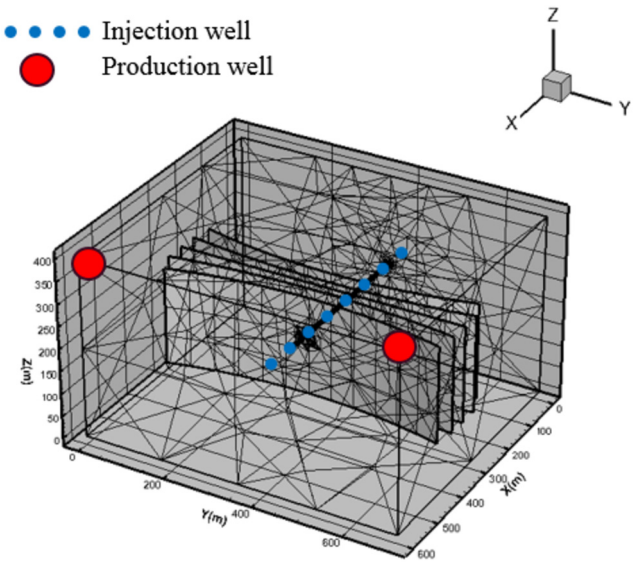

Fig. 8. Domain and mesh (2500 element mesh used in this figure for demonstration); dotted line in the middle represent the well crossing four non-planar fractures: Example 3.

Table 2
Oil composition: Example 3.

Component	Overall mole fraction
CO_2	0.0086
N_2	0.0028
C_1	0.4451
C_2-C_3	0.1207
C_4-C_5	0.0505
C_6-C_{10}	0.1328
C_{11}-C_{24}	0.166
C_{25+}	0.0735

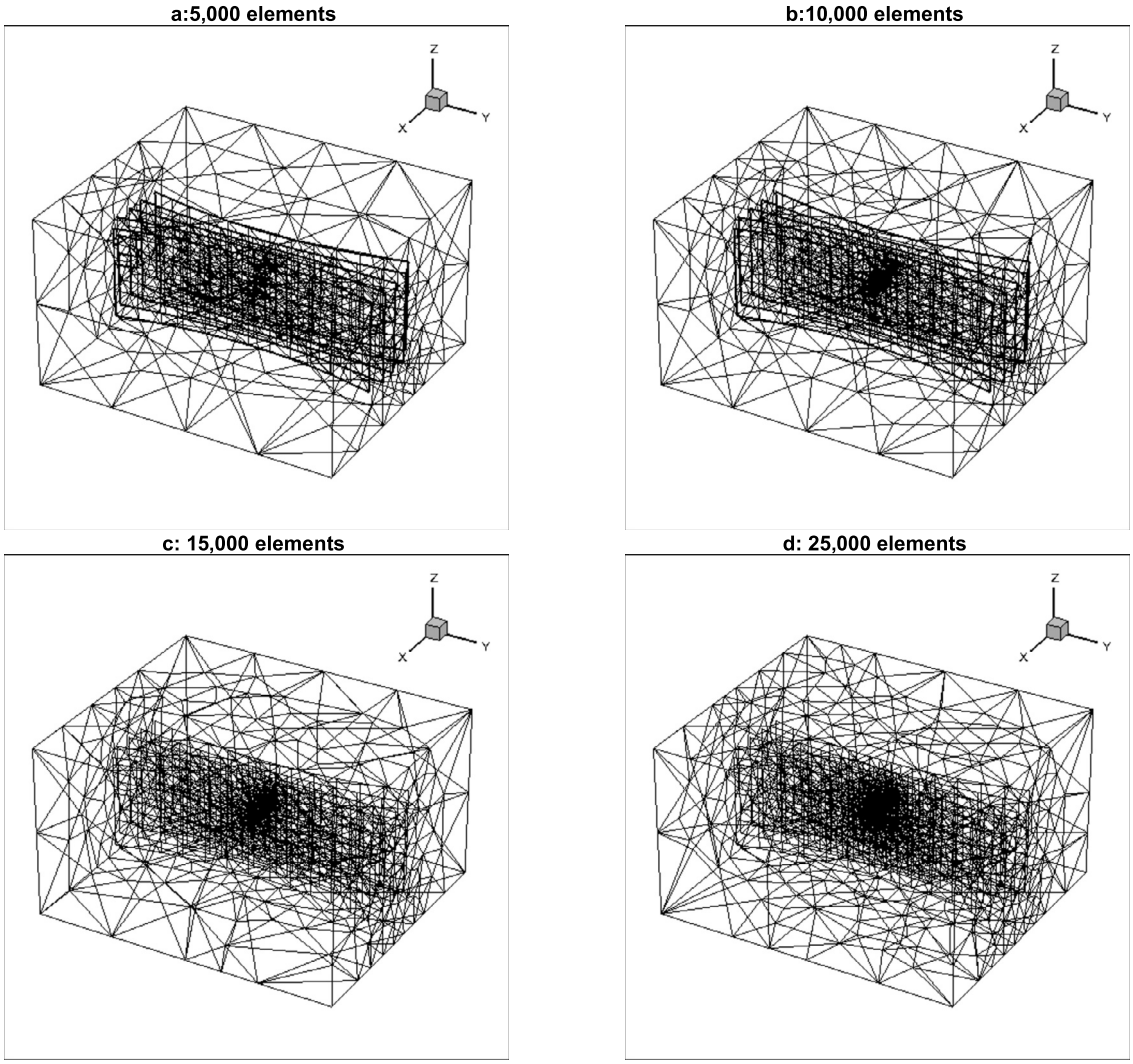

Fig. 9. Different meshes: Example 3.

Table 3
Relevant data: Example 3.

Property	Value
Matrix permeability [md]	100
Porosity [%]	20
Temperature [K]	403.15
Pressure at the bottom [bar]	276
Fracture width [mm]	1
Fracture permeability [md]	10^6

The total volume balance in the pressure equation is given by [1,33]:

$$\phi C_t \frac{\partial p}{\partial t} + \sum_{i=1}^{n_c} \bar{V}_i \nabla . \left(\sum_{\alpha} c_\alpha x_{i,\alpha} \boldsymbol{v}_\alpha \right) = \sum_{i=1}^{n_c} \bar{V}_i F_i \tag{4}$$

where C_t is the total compressibility and $\bar{V}_i$ is the total partial molar volume of component i [10].

Calculation of phase equilibrium is based on initial guess from stability analysis and the minimum of Gibbs free energy. The phase and volumetric behavior and the local thermodynamic equilibrium imply:

$$\begin{cases} f_{i,o}(T,p,x_{j,o}) = f_{i,g}(T,p,x_{j,g}), \quad i = 1,..n_c;\ j = 1,..n_c - 1 \\ Z_\alpha^3 - (1 - B_\alpha) Z_\alpha^2 + (A_\alpha - 3B_\alpha^2 - 2B_\alpha) Z_\alpha - (A_\alpha B_\alpha - B_\alpha^2 - B_\alpha^3) = 0 \end{cases} \tag{5}$$

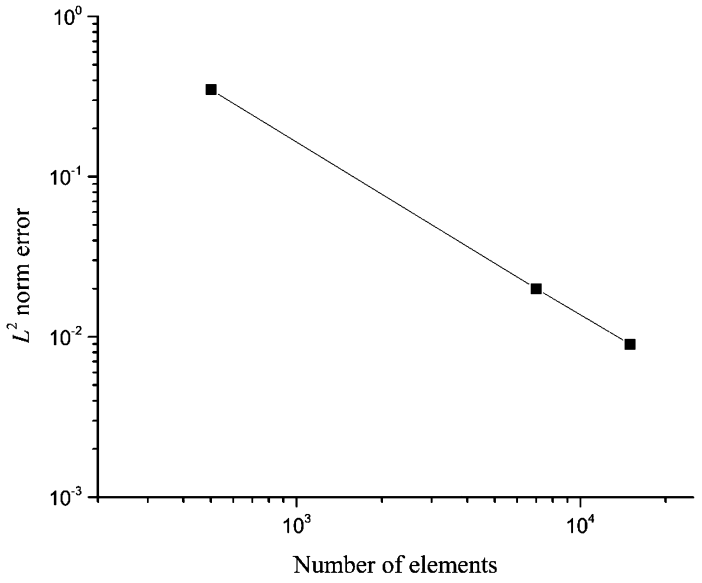

Fig. 10. L^2 norm of error in gas saturation: Example 3.

A_α, B_α are the parameters of the Peng-Robinson equation of state (PR-EOS) which depend on pressure, temperature and composition of each phase [26].

Fracture network

The mass balance equations in the fracture elements are given by:

$$\phi \frac{\partial cz_i}{\partial t} + \nabla . \left(\sum_\alpha c_\alpha x_{i,\alpha} \left(\boldsymbol{v}_\alpha - \boldsymbol{v}_\alpha^{fr} \right) \right) = F_i, \quad i = 1 \ldots n_c \tag{6}$$

$\boldsymbol{v}_\alpha$ is the velocity across the fracture width, and $\boldsymbol{v}_\alpha^{fr}$ is the velocity along the fracture length.

The pressure equation in the fractures is given by:

$$\phi C_t \frac{\partial p}{\partial t} + \sum_{i=1}^{n_c} \bar{V}_i \left[\nabla . \left(\sum_\alpha c_\alpha x_{i,\alpha} \left(\boldsymbol{v}_\alpha - \boldsymbol{v}_\alpha^{fr} \right) \right) - F_i \right] = 0 \tag{7}$$

Numerical scheme

The hybridized mixed finite element (MFE) method is used to solve for the flow [14,41,43]. The pressure at the cell centers and the traces of pressure at the cell interfaces are evaluated with the MFE method which leads to accurate flux calculation in unstructured gridding [20,12,40,42,56–58,54,55]. In the fractures we use the finite volume (FV) discretization method, and in the matrix domain we use the discontinuous Galerkin method (DG) to solve for the mass balance equations. DG is a method of choice to capture the discontinuities in phase composition at the element interfaces.

The fluxes are evaluated at the interfaces of all FE as follows:

$$q_{K,E} = \alpha_{K,E} p_K - \sum_{E' \in \partial K} \beta_{K,E,E'} t p_{K,E'} - \gamma_{K,E} \tag{8}$$

The coefficients $\alpha_{K,E}$, $\beta_{K,E,E'}$ and $\gamma_{K,E}$ depend on the geometry of the element; details of the MFE formulation can be found in [4,3].

The FV integration of the pressure equation in the matrix domain gives:

$$\phi |K| C_t \frac{\Delta p}{\Delta t} + \sum_{i=1}^{n_c} \bar{V}_{i,K} \left[\sum_\alpha \sum_{E \in \partial K} \int_E c_\alpha x_{i,\alpha} f_\alpha (\boldsymbol{v} + \boldsymbol{G}_\alpha) . \boldsymbol{n}_E - F_{i,K} \right] = 0 \tag{9}$$

In the fracture network we get:

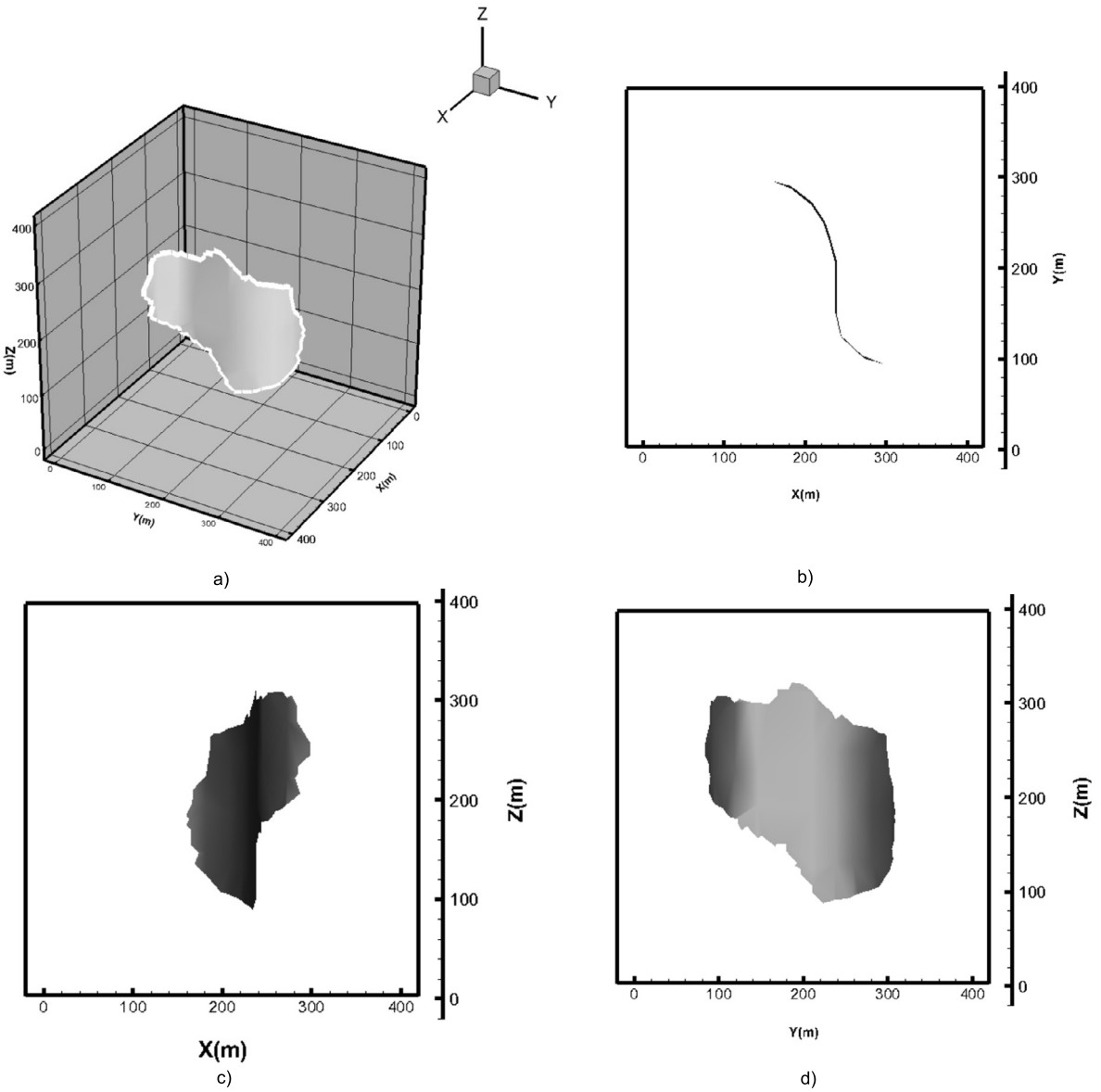

Fig. 11. Perspective view (a) and XY (b), XZ (c) and YZ (d) projections of fracture F1: Example 4.

$$\phi C_t |k| \frac{\Delta p}{\Delta t} + \sum_{i=1}^{n_c} \bar{V}_{i,k} \left[\sum_e \int_e \sum_\alpha c_\alpha x_{i,\alpha} f_\alpha (\boldsymbol{v} + \boldsymbol{G}_\alpha).\boldsymbol{n}_e - \sum_{Ei} \int_{Ei} \sum_\alpha c_\alpha x_{i,\alpha} \boldsymbol{v}_\alpha^{fr}.\boldsymbol{n}_{Ei} - |k| F_i \right] = 0 \tag{10}$$

The DG discretization of the mass balance equations in the matrix domain and the FV discretization in the fracture network are given in the following two equations, respectively:

$$\int_K \phi \frac{\partial c z_i}{\partial t} \varphi_{K,j} + \sum_E \int_E \sum_\alpha (\overline{c_\alpha x_{i,\alpha}} \boldsymbol{v}_\alpha) n_E \varphi_{K,j} - \int_K \sum_\alpha (c_\alpha x_{i,\alpha} \boldsymbol{v}_\alpha) \nabla \varphi_{K,j} = \int_K F_i \varphi_{K,j} \tag{11}$$

$$\phi |k| \frac{c z_{i,k}^{n+1} - c z_{i,k}^{n}}{\Delta t} + \sum_\alpha \left(\sum_{e \in \partial k} (\overline{c_\alpha x_{i,\alpha}}^{n+1} q_{\alpha,k,e}) - \overline{Q}_{\alpha,i}^{fr} \right) = |k| F_i \tag{12}$$

More details of the term $\overline{Q}_{\alpha,i}^{fr}$ that represent the exchange flux of component i in phase α between the fracture and the adjacent matrix elements are given in [53]. All the symbols are defined in the nomenclature. To remove the non-physical

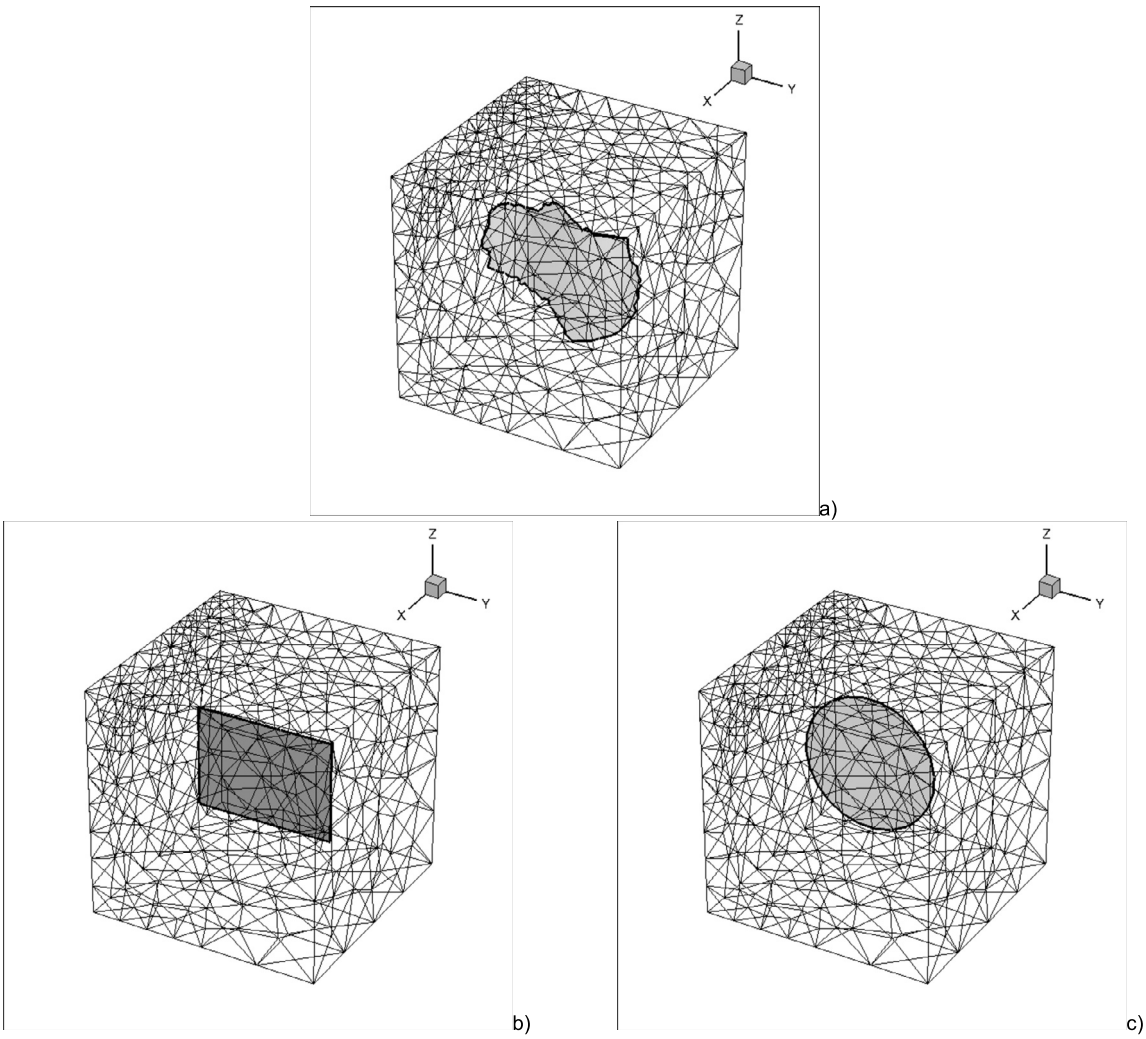

Fig. 12. Different fracture shapes F1 (a), F2 (b) and F3 (c) shown in a 5,000 elements mesh: Example 4.

oscillations of higher-order method, we apply a multidimensional slope limiter to reconstruct the solution over the simulation domain [13]. The time step selection is based on the CFL condition in the matrix domain. The implicit scheme in the fractures allows to avoid the severe CFL restriction in small fracture elements.

In the formulation in this work we neglect capillary pressure and physical diffusion.

Examples

We present five numerical examples where the number of components in the petroleum fluid varies from 2 to 8. We use quadratic function of saturation for relative permeabilities in all runs.

Example 1: mesh dependency

Under complex stress conditions, fractures could propagate in 3D non-predefined paths [25]. As a result, non-planar fractures and cracks are created. Paul et al. [25] studied the fractures propagation under different stress conditions. In this example we simulate a non-planar fracture shape similar to [25]. The fracture shape in [25] is developed inside a block exposed to a horizontal stress in one direction. We consider the domain of $300 \times 150 \times 200$ m^3 size. The domain and the fracture are shown in Fig. 2. We inject methane into a formation saturated with propane. Injection is performed at one corner and production at constant pressure at the opposite corner. Relevant data of the problem are given in Table 1. To study the effect of mesh dependency we consider 4 different mesh refinements of 2500, 5000, 10000 and 20000 elements that we denote by mesh: a, b, c and d, respectively. The oil recovery in four meshes gives a good agreement in production

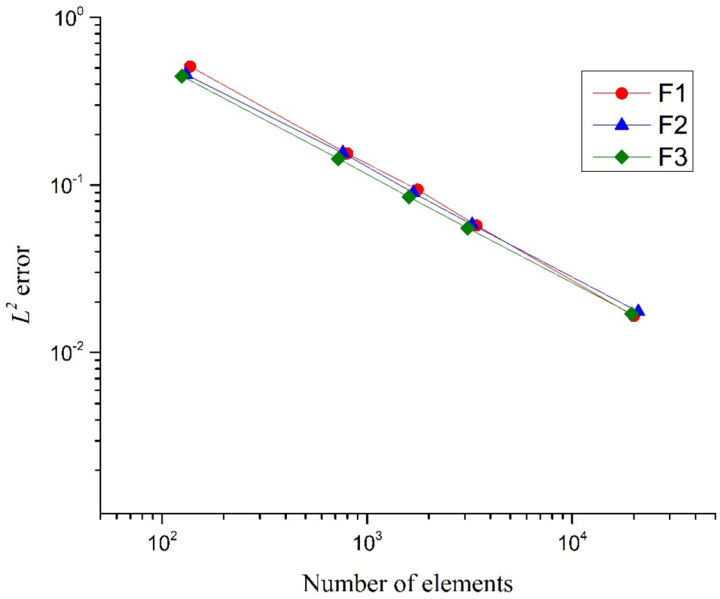

Fig. 13. Relative L^2 norm of error in gas saturation for three different fracture shapes: Example 4.

Table 4
Order of convergence (OC) in different fracture shapes: Example 4.

Fracture	p(OOC)
F1	0.66
F2	0.74
F3	0.77

profiles even for a relatively coarse mesh of 2500 for such a 3D complex system (Fig. 3). For reference we show the gas saturation at different pore volume injections (PVI) in Fig. 4.

Example 2: impermeable fault

One advantage of our algorithm compared to other approaches is the ease of simulation of all range of fracture permeability values. The fractures in our model are represented by the interfaces of matrix finite elements. This allows to readily assign zero permeability for some fractures; making the elements as impermeable faults. We consider in this example the same properties as in Example 1 except the fracture permeability is set to zero. We compare the oil recovery with different mesh refinements (same meshes as in Example 1), and as shown in Fig. 5 a good agreement is observed. The agreement in oil recovery for all meshes is better than in Example 1 since the elements belonging to the faults do not contribute to flow. The flow is therefore numerically updated through the higher-order scheme in the matrix elements only. For reference we show the gas saturation at different PVI in Fig. 6.

We have also simulated the same problem with a non-planar fracture and an impermeable fault (Examples 1 and 2) with different shapes (see Fig. 7). Results for those runs are not shown for the sake of brevity. They are consistent with what we observe in Figs. 3 and 5 revealing the accuracy of our algorithm.

Example 3: horizontal well

Fracture growth is affected by the in-situ compressive stress and the fluid pressure. Xu and Wong [38] proposed a 3D model for growth of hydraulic fractures. In their work they reported the formation and growth of four non-planar fractures in a domain with one horizontal well. We consider a similar example as in [38]. We have designed four non-planar fractures with one horizontal well in a $600 \times 650 \times 400$ m^3 domain (Fig. 8).

CO_2 is injected through the horizontal well into a matrix saturated with an 8-component oil and production is at constant pressure at the top two opposite corners of the domain. The oil composition is shown in Table 2, and the relevant data of the problem are provided in Table 3.

We evaluate the relative L^2 norm of error in gas saturation in 3 different meshes of 5,000, 10,000, and 15,000 elements, respectively; a more refined mesh of 25,000 elements is used as a reference solution mesh. The four different meshes are shown in Fig. 9.

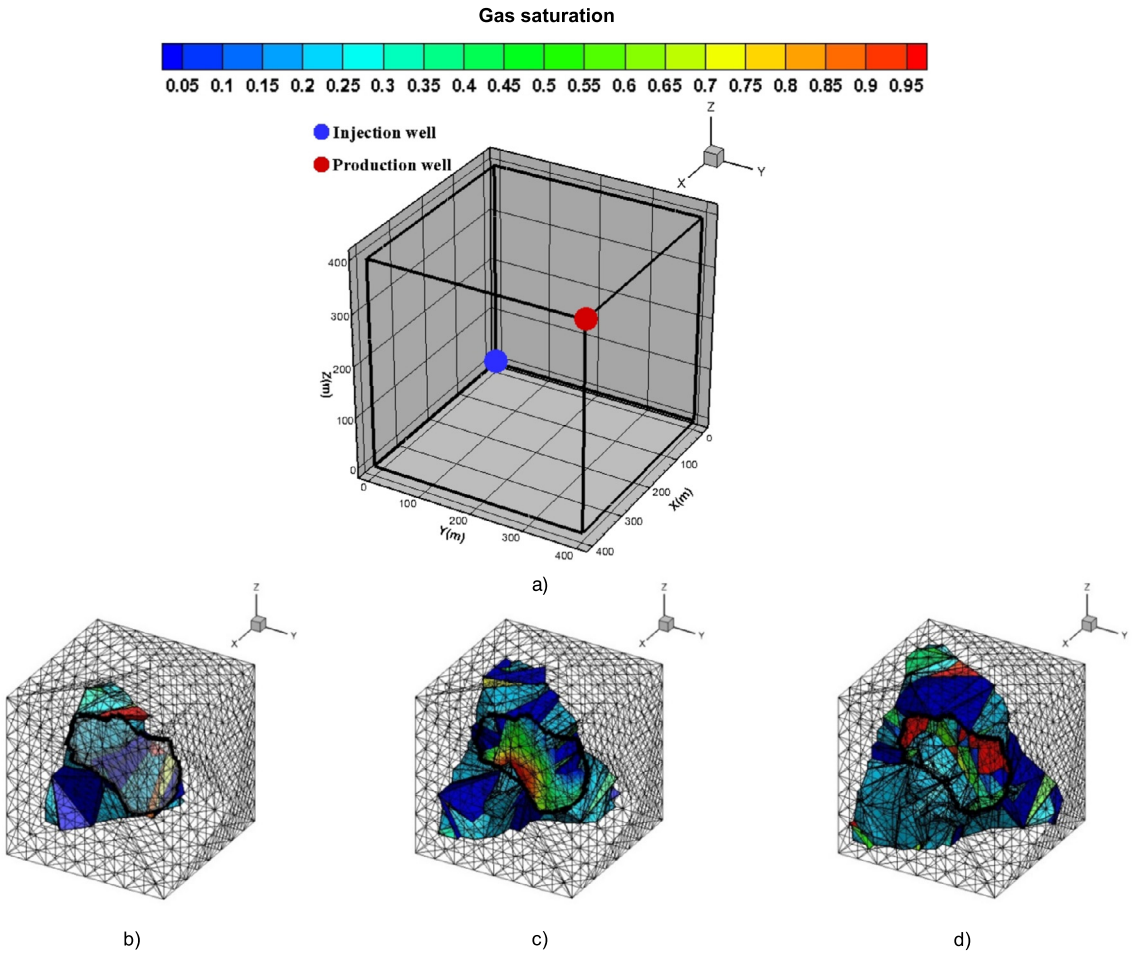

Fig. 14. Location of injection and production wells, fracture is removed for clarity (a); Gas saturation at 10% (b), 20% (c), 30% (d) PVI in the 10,000-element mesh: Example 4.

The error in gas saturation reduces from 8% in a relatively coarse mesh to less than 4% for the 15,000 element mesh as shown in Fig. 10. This demonstrates the convergence in our model without an excessive mesh refinement.

Example 4: fracture shape and algorithm accuracy

We study the effect of fracture shape on relative L^2 norm of error. We consider a cubic domain of 400 m side length in three different scenarios. In each of the three scenarios a different fracture shape is designed. The first fracture shape is motivated from the experimental work of Zhu et al. [50] in hydraulic fracturing. The fracture shape (denoted by F1) is shown in Fig. 11. The two other fracture shapes (quadrangular shape in 3D, denoted by F2 and circular shape, denoted by F3) are shown in Fig. 12 with the corresponding mesh discretization. The properties of the domain and the oil are the same as in Example 3. CO_2 is injected at one corner and production is from the opposite corner of the domain. To compare the error for the three scenarios, we have placed the fractures in the middle of the domain; all three fractures have the same surface area. Therefore, the error difference is strictly related to the fracture shape. The L^2 norm of error in gas saturation is calculated at different mesh refinements from 100 to 30000 elements in all cases. Results show (Fig. 13) a similar profile in L^2 of norm error that decreases to less than 5% in all three scenarios. In Table 4 we show the order of convergence (OOC) for all the fracture shapes (F1, F2 and F3). The order of convergence (p) is calculated in terms of L^2 norm of error using Eq. (13) where N is the number of elements, S_r is a reference solution, C is a constant and r is a refinement parameter. For reference we show the gas saturation at different PVI for the complex fracture shape (F1) in Fig. 14.

$$\left(\sum_{N}(S - S_r)^2\right)^{1/2} \leq (Cr)^p \tag{13}$$

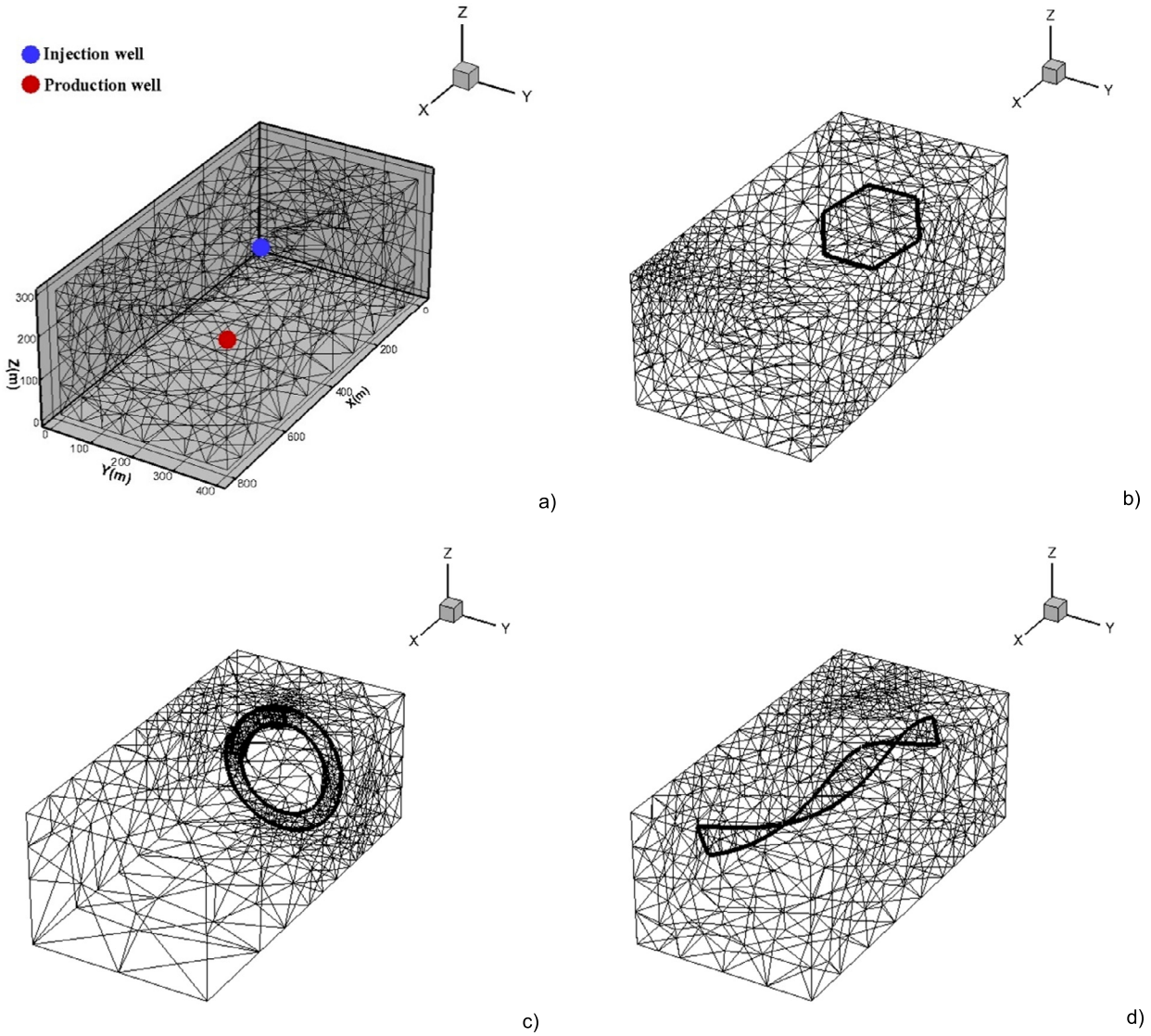

Fig. 15. Location of injection and production wells, fracture removed to show location of the wells (a) and the three fracture shapes, F1 (b), F2 (c) and F3 (d), 6000 elements mesh is used: Example 5.

Example 5: non-planar fracture and oil recovery

In the last example we study the effect of the fracture shape on oil recovery. Three different fracture shapes are considered, two non-planar shapes and one polygonal planar fracture. The three fractures are independently located in the same matrix domain that has a size of $800 \times 400 \times 300$ m^3. The domain and the three fracture shapes (F1, F2, F3) are shown in Fig. 15. All the fractures (F1-F3) have the same surface area (of 34000 m^2) in order to compare the recovery in the three different cases. The relevant data of the problem are the same as in Example 4. The number of elements in the matrix and the fractures in the three scenarios are kept within the range of 5000 elements for the matrix and 1000 elements in the fractures. We show in Fig. 16 the perspective view and projections of the three fractures.

We show in Fig. 17 the oil recovery in different fracture shapes (F1-F3). The recovery profiles show that the highest recovery is from F2 and the lowest from F1. The shape of fracture F2 is not aligned with the injection-production pressure gradient, hence the injected gas reaches the reservoir limits before being produced. In the fracture shape F3, the twists along the total fracture length makes most of the gas flow towards the matrix domain. The planar fracture F1, however, is oriented at an angle that the injected gas flows in a favorable direction within the injection-production pressure gradient leading to early breakthrough compared to F2 and F3 and therefore lower recovery. A planar or non-planar fracture does not necessarily imply a lower or higher production performance. The shape and orientation of the fracture could favor

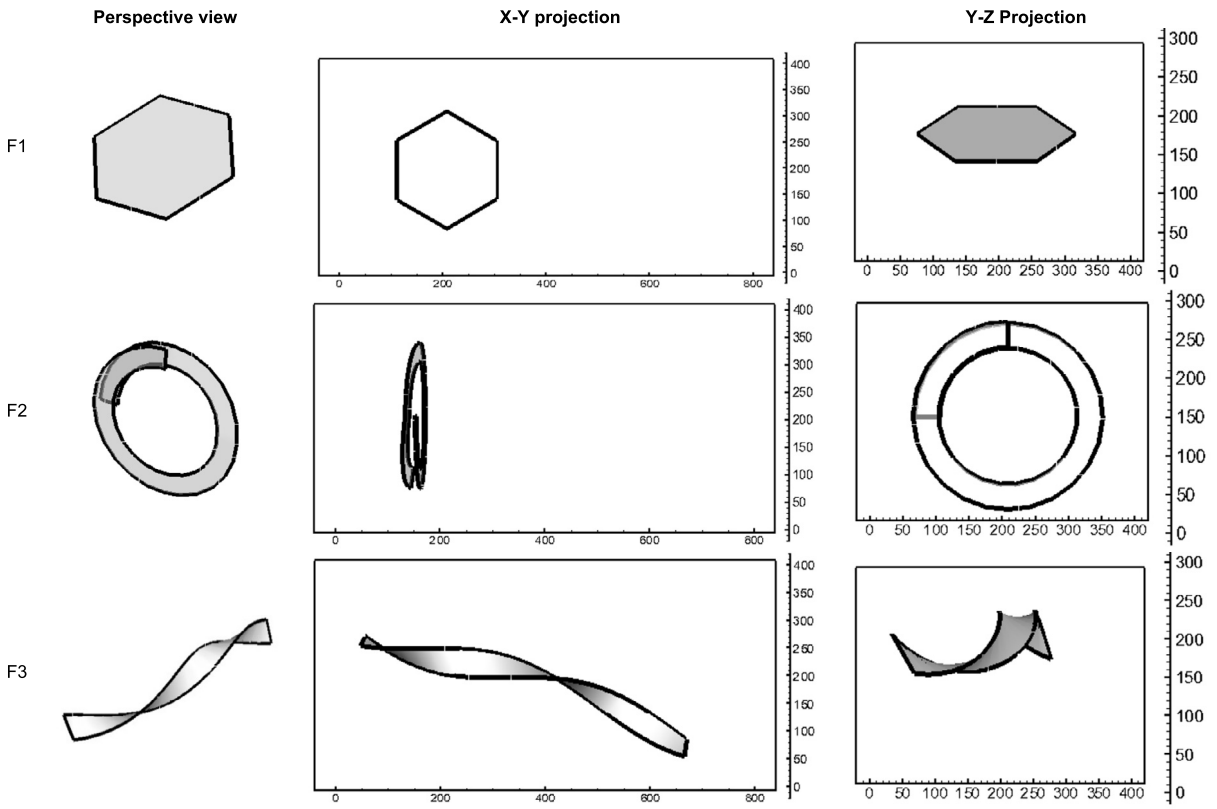

Fig. 16. Perspective view and projections of fractures F1, F2, and F3: Example 5. Distances in meter.

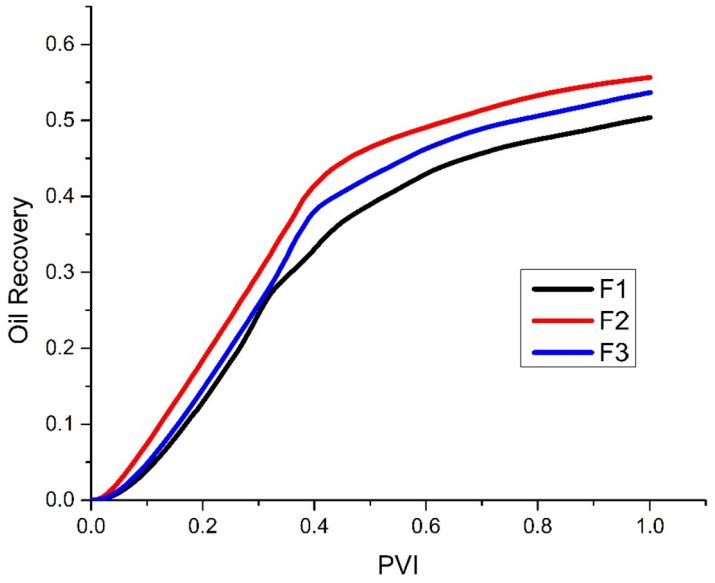

Fig. 17. Oil recovery in different fracture shapes: Example 5.

the reservoir reach to improve well performance or lead to early breakthrough. For reference we show in Fig. 18 the gas saturation in the three cases at different PVI.

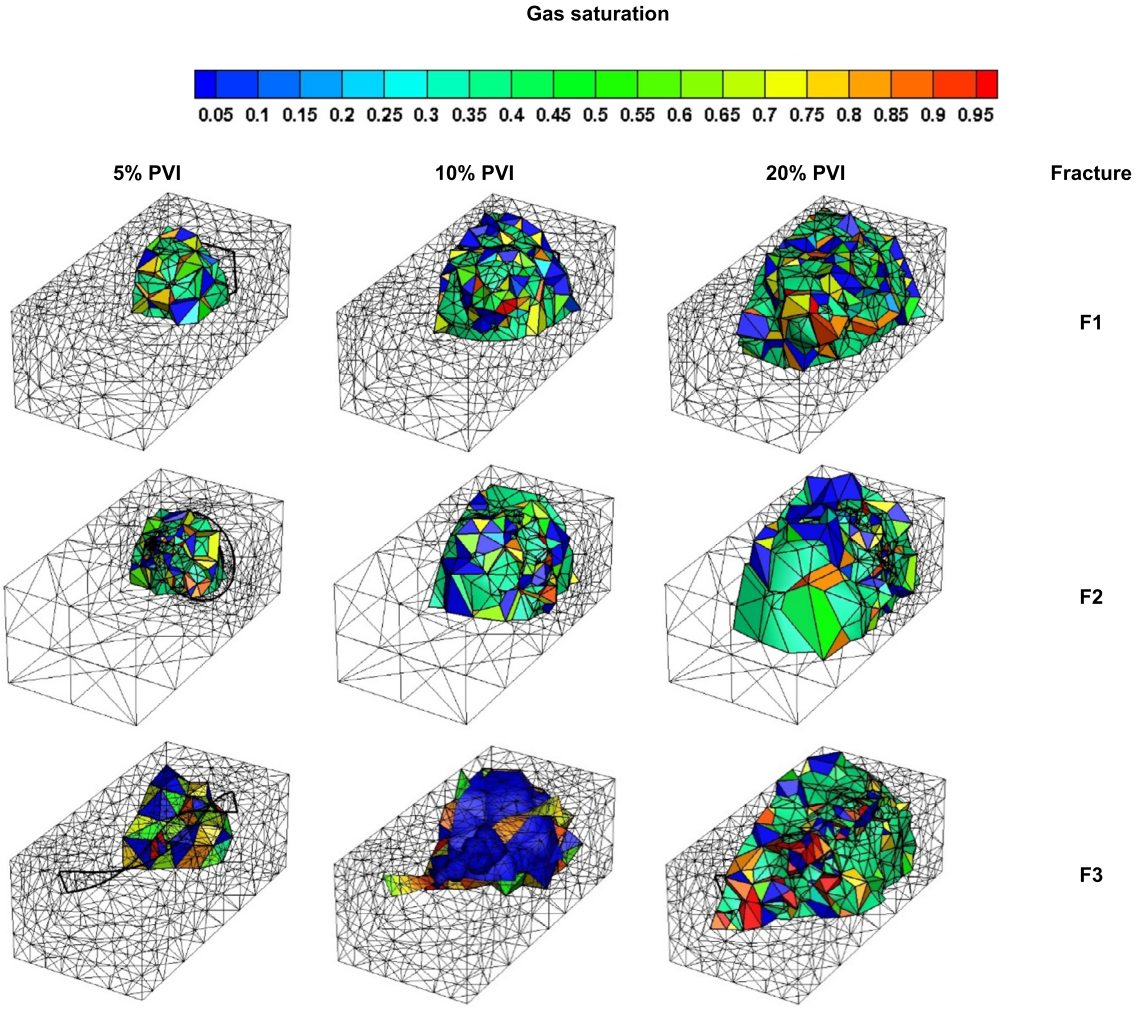

Fig. 18. Gas saturation at different PVI; 6,000 elements mesh is used: Example 5.

Summary and concluding remarks

We present an efficient algorithm for simulation of compositional two-phase flow in a domain containing non-planar fractures. A set of tools are developed to design and mesh the most complicated fracture geometries in 3D. This is achieved by the interfaces we have developed in the CAD framework and the unstructured tetrahedrons. In our work we can choose different refinements at and near the fractures based on the complexity of fracture shape and the order of accuracy. Our simulation shows low mesh dependency in the 3D complex domains. We demonstrate that the complexity of the fracture shape does not affect the accuracy of the algorithm. Simulation of transport in non-planar fractures is based on the FCFE approach that alleviates the restriction on the time step imposed by small fracture grid cells in the domain. All range of fracture permeability values can be simulated in our model and fractures can be readily set to impermeable faults. This feature will allow to use a wide range of permeability values in different parts of a given fracture. We have shown in the examples that a non-planar fracture does not necessarily imply a lower production performance.

The work presented in this paper does not include the mechanics of the fracturing and fracture roughness. It sets stage to investigate fracturing by water and by CO_2

Nomenclature

c overall molar density of the mixture
C_t total compressibility
c_α molar density
E grid edge
F_i sink/source term

f_α fractional flow function
$f_{\alpha,i}$ fugacity
g gas phase
$\mathbf{g}$ gravitational acceleration
i component index
K grid element
$|K|$ volume of matrix grid cell
$|k|$ volume of fracture grid cell
$\mathbf{K}$ absolute permeability
$k_{r\alpha}$ relative permeability
n_c number of components
N number of elements
$\boldsymbol{n}_E$ outward normal vector
o oil phase
p pressure, also order of convergence (OOC)
$q_{K,E}$ total flux across edge E in element K
$\overline{Q}^{fr}_{\alpha,i}$ matrix-fracture exchange flux
T temperature
$\bar{V}_i$ total partial molar volume
$\boldsymbol{v}_\alpha$ velocity of phase α
$\boldsymbol{v}^{fr}_\alpha$ velocity across the fracture length
$x_{i,\alpha}$ mole fraction
z_i overall mole fraction
α phase index
Ω computational domain
τ simulation time
μ_α dynamic viscosity
ρ_α mass density
ϕ porosity
λ_α mobility of phase α
$\varphi_{K,j}$ DG basis function
Δt time step

Declaration of competing interest

The authors declare that they have no known competing financial interests or personal relationships that could have appeared to influence the work reported in this paper.

Acknowledgement

This work was supported by the member companies of the Reservoir Engineering Research Institute (RERI) whose support is gratefully acknowledged.

References

[1] G. Acs, S. Doleschall, E. Farkas, General purpose compositional model, SPE J. 25 (4) (1985) 543–553, https://doi.org/10.2118/10515-PA.
[2] T. Belytschko, T. Black, Elastic crack growth in finite element with minimal remeshing, Int. J. Numer. Methods Eng. 45 (1999) 601–620, https://doi.org/10.1002/(SICI)1097-0207.
[3] G. Chavent, J.E. Roberts, A unified physical presentation of mixed, mixed-hybrid finite element method and standard finite difference approximations for the determination of velocities in water flow problems, Adv. Water Resour. 14 (6) (1991) 329–348, https://doi.org/10.1016/0309-1708(91)90020-O.
[4] G. Chavent, G. Cohen, J. Jaffré, R. Eyard, D.R. Guerillot, L. Weill, Discontinuous and mixed finite elements for two-phase incompressible flow, SPE Reserv. Eng. 5 (4) (1990) 567–575, https://doi.org/10.2118/16018-PA.
[5] B. Carrier, S. Granet, Numerical modeling of hydraulic fracture problem in permeable medium using cohesive zone model, Eng. Fract. Mech. 79 (2012) 312–328, https://doi.org/10.1016/j.engfracmech.2011.11.012.
[6] C.L. Cipolla, T. Fitzpatrick, M.J. Williams, U.K. Ganguly, Seismic-to-simulation for unconventional reservoir development, in: SPE Reservoir Characterisation and Simulation Conference and Exhibition, Society of Petroleum Engineers, 2011, SPE-146876-MS.
[7] A. Cornec, I. Scheider, K.H. Schwalbe, On the practical application of the cohesive model, Eng. Fract. Mech. 70 (1963) 1963–1987, https://doi.org/10.1016/S0013-7944(03)00134-6.
[8] A. Dahi-Taleghani, J.E. Olson, Numerical modeling of multistranded-hydraulic-fracture propagation: accounting for the interaction between induced and natural fractures, SPE J. 16 (2011) 575–581, https://doi.org/10.2118/124884-PA, SPE-124884-PA.
[9] J.S. Filho, K. Kamy Sepehrnoori, Simulation of planar hydraulic fractures with variable conductivity using the embedded discrete fracture model, J. Pet. Sci. Eng. 153 (2017) 212–222, https://doi.org/10.1016/j.petrol.2017.03.049.
[10] A. Firoozabadi, Thermodynamics and Applications of Hydrocarbons Energy Production, McGraw-Hill Professional, 2015.

[11] P. Gupta, C.A. Duarte, Simulation of non-planar three-dimensional hydraulic fracture propagation, Int. J. Numer. Anal. Methods Geomech. 38 (2014) 1397–1430, https://doi.org/10.1002/nag.2305.
[12] H. Hoteit, A. Firoozabadi, An efficient model for incompressible two-phase flow in fractured media, Adv. Water Resour. 31 (2008) 891–905, https://doi.org/10.1016/j.advwatres.2008.02.004.
[13] H. Hoteit, P. Ackerer, R. Mosé, Nuclear waste disposal simulations: couplex test cases, Comput. Geosci. 8 (2) (2004) 99–124, https://doi.org/10.1023/B:COMG.0000035074.37722.71.
[14] P. Huggenberger, A. Zidane, E. Zechner, D. Gechter, The role of tectonic structures and density-driven groundwater flow for salt karst formation, Eng. Geol. Soc. Territ. 5 (2015) 609–612, https://doi.org/10.1007/978-3-319-09048-1_118.
[15] I. Ispas, R. Eve, R.J. Hickman, R.G. Keck, S.M. Willson, K.E. Olson, Laboratory testing and numerical modelling of fracture propagation from deviated wells in poorly consolidated formations, SPE J. 3 (2012) 56–61, https://doi.org/10.2118/159262-MS.
[16] X. Li, Z. Feng, G. Han, D. Elsworth, C. Marone, D. Saffer, D.S. Cheon, Breakdown pressure and fracture surface morphology of hydraulic fracturing in shale with H_2O, CO_2 and N_2, Geomech. Geophys. Geo-Energy Geo-Resour. 2 (2016) 63–76, https://doi.org/10.1007/s40948-016-0022-6.
[17] J. Lohrenz, B.G. Bray, C.R. Clark, Calculating viscosities of reservoir fluids from their compositions, J. Pet. Technol. 16 (10) (1964) 1171–1176, https://doi.org/10.2118/915-PA.
[18] N. Moes, J. Dolbow, T. Belytschko, A finite element method for crack growth without remeshing, Int. J. Numer. Methods Eng. 46 (1999) 131–150, https://doi.org/10.1002/(SICI)1097-0207.
[19] M.M. Molenaar, E. Fidan, D. Hill, Real-time downhole monitoring of hydraulic fracturing treatments using fibre optic distributed temperature and acoustic sensing, in: SPE, EAGE European Unconventional Resources Conference and Exhibition, 2012.
[20] R. Mosé, P. Siegel, P. Ackerer, G. Chavent, Application of the mixed hybrid finite element approximation in a ground water flow model: luxury or necessity? Water Resour. Res. 30 (11) (1994) 3001–3012, https://doi.org/10.1029/94WR01786.
[21] P.N. Mutalik, R.W. Gibson, Case history of sequential and simultaneous fracturing of the Barnett Shale in Parker County, in: SPE Annual Technical Conference and Exhibition, 2008.
[22] J. Noorishad, C.F. Tsang, P. Witherspoon, Theoretical and field studies of coupled hydromechanical behavior of fractured rocks -1. Development and verification of a numerical simulator, Int. J. Rock Mech. Min. Sci. Geomech. Abstr. 29 (1992) 401–409, https://doi.org/10.1016/0148-9062(92)90515-2.
[23] J.E. Olson, Fracturing from highly deviated and horizontal wells: numerical analysis of non-planar fracture propagation, in: Low Permeability Reservoirs Symposium, 1995.
[24] J. Olson, Multi-fracture propagation modeling: applications to hydraulic fracturing in shales and tight gas sands, in: The 42nd US Rock Mechanics Symposium (USRMS), American Rock Mechanics Association, 2008 (29), ARMA-08-327.
[25] B. Paul, M. Faivre, P. Massin, R. Giot, D. Colombo, F. Golfier, A. Martin, 3D coupled HM-XFEM modeling with cohesive zone model and applications to non-planar hydraulic fracture propagation and multiple hydraulic fractures interference, Comput. Methods Appl. Mech. Eng. 342 (2018) 321–353, https://doi.org/10.1016/j.cma.2018.08.009.
[26] D.Y. Peng, D.B. Robinson, A new two-constant equation of state, Ind. Eng. Chem. Fundam. 15 (1976) 59–64.
[27] H. Si, TetGen: a quality tetrahedral mesh generator and a 3D delaunay triangulator, http://wias-berlin.de/software/tetgen/, 2011.
[28] J.R. Sierra, J.D. Kaura, D. Gualtieri, G. Glasbergen, D. Sarker, D. Johnson, DTS monitoring of hydraulic fracturing: experiences and lessons learned, in: SPE Annual Technical Conference and Exhibition, 2008.
[29] R.G. Van de Ketterij, C.J. de Pater, Experimental study on the impact of perforations on hydraulic fracture tortuosity, in: SPE European Formation Damage Conference, 1997.
[30] R.G. Van de Ketterij, C.J. de Pater, Numerical simulations of hydraulic fracture link-up of perforations at deviated wellbores, in: SPE European Formation Damage Conference, 1999.
[31] C.A.M. Veeken, D.R. Davies, J.V. Walter, Limited communication between hydraulic fracture and (deviated) wellbore, in: Low Permeability Reservoirs Symposium, 1989.
[32] G.A. Waters, B.K. Dean, R.C. Downie, K.J. Kerrihard, L. Austbo, B. McPherson, Simultaneous hydraulic fracturing of adjacent horizontal wells in the Woodford shale, in: SPE Hydraulic Fracturing Technology Conference, 2009.
[33] J.W. Watts, A compositional formulation of the pressure and saturation equations, SPE Reserv. Eng. 1 (3) (1986) 243–252, https://doi.org/10.2118/12244-PA.
[34] X. Weng, O. Kresse, C. Cohen, R. Wu, H. Gu, Modeling of hydraulic-fracture-network propagation in a naturally fractured formation, SPE Prod. Oper. 26 (2011) 368–380, https://doi.org/10.2118/140253-PA.
[35] X. Weng, Fracture initiation and propagation from deviated wellbores, in: SPE Annual Technical Conference and Exhibition, 1993.
[36] K. Wu, J.E. Olson, Investigation of the impact of fracture spacing and fluid properties for interfering simultaneously or sequentially generated hydraulic fractures, SPE Prod. Oper. 28 (2013) 427–436, https://doi.org/10.2118/163821-PA.
[37] K. Wu, J.E. Olson, Mechanics analysis of interaction between hydraulic and natural fractures in shale reservoirs, in: SPE/AAPG/SEG Unconventional Resources Technology Conference, 2014.
[38] G. Xu, S.-W. Wong, Interaction of multiple non-planar hydraulic fractures in horizontal wells, in: International Petroleum Technology Conference, 2013.
[39] K. Yamamoto, T. Shimamoto, S. Sukemura, Multiple fracture propagation model for a three-dimensional hydraulic fracturing simulator, Int. J. Geomech. 4 (2004) 46–57, https://doi.org/10.1061/(ASCE)1532-3641(2004)4:1(46).
[40] A. Younes, M. Konz, M. Fahs, A. Zidane, P. Huggenberger, Modelling variable density flow problems in heterogeneous porous media using the method of lines and advanced spatial discretization methods, Math. Comput. Simul. 81 (2011) 2346–2355, https://doi.org/10.1016/j.matcom.2011.02.010.
[41] A. Younes, M. Fahs, B. Belfort, Monotonicity of the cell-centred triangular MPFA method for saturated and unsaturated flow in heterogeneous porous media, J. Hydrol. 504 (2013) 132–141, https://doi.org/10.1016/j.jhydrol.2013.09.041.
[42] A. Younes, A. Markadi, A. Zidane, Q. Shao, L. Bouhala, A combination of Crouzeix-Raviart, discontinuous Galerkin and MPFA methods for buoyancy-driven flows, Int. J. Numer. Methods Heat Fluid Flow 3 (24) (2014) 735–759, https://doi.org/10.1108/HFF-07-2012-0156.
[43] A. Younes, M. Fahs, A. Zidane, P. Huggenberger, E. Zechner, A new benchmark with high accurate solution for hot–cold fluids mixing, Heat Mass Transf. 9 (51) (2015) 321–1336, https://doi.org/10.1007/s00231-015-1500-z.
[44] X. Zhang, Y. Lu, J. Tang, Z. Zhou, Y. Liao, Experimental study on fracture initiation and propagation in shale using supercritical carbon dioxide fracturing, Fuel 190 (2017) 370–378, https://doi.org/10.1016/j.fuel.2016.10.120.
[45] R.X. Zhang, B. Hou, Q.Y. Zhang, X.W. Zhou, Q.L. Shan, X. Liu, Experimental study on hydraulic fracture non-planar propagation from perforated horizontal well in tight formations, in: 52nd U.S. Rock Mechanics/Geomechanics Symposium, 2018, ARMA-2018-057.
[46] G. Zhang, Y. Yudong Zhang, A. Xu, Y. Li, Microflow effects on the hydraulic aperture of single rough fractures, Adv. Geo-Energy Res. 3 (2019) 104–114, https://doi.org/10.26804/ager.2019.01.09.
[47] D. Zhou, G. Zhang, Y. Wang, Y. Xing, Experimental investigation on fracture propagation modes in supercritical carbon dioxide fracturing using acoustic emission monitoring, Int. J. Rock Mech. Min. Sci. 110 (2018) 111–119, https://doi.org/10.1016/j.ijrmms.2018.07.010.
[48] D. Zhou, G. Zhang, P. Zhao, Y. Wang, S. Xu, Effects of post-instability induced by supercritical CO_2 phase change on fracture dynamic propagation, J. Pet. Sci. Eng. 162 (2018) 358–366, https://doi.org/10.1016/j.petrol.2017.12.066.
[49] S. Zhou, S. Raj Banerjee, S. Bobby Poe, S. Je_Spath, M.S. Thambynayagam, Semi-analytical production simulation of complex hydraulic fracture networks, SPE J. 19 (01) (2014) 6–18, https://doi.org/10.2118/157367-PA.

[50] H.Y. Zhu, J.G. Deng, S.J. Liu, W. Min, P.Y. Cheng, L.R. Ji, C.J. Zi, H.B. Lian, L. Hai, G. Dong, Hydraulic fracturing experiments of highly deviated well with oriented perforation technique, Geomech. Geoengin. (6) (2014) 153–172, https://doi.org/10.12989/gae.2014.6.2.153.
[51] A. Zidane, A. Firoozabadi, An efficient numerical model for multicomponent compressible flow in fractured porous media, Adv. Water Resour. 74 (2014) 127–147, https://doi.org/10.1016/j.advwatres.2014.08.010.
[52] A. Zidane, A. Firoozabadi, An implicit numerical model for multicomponent compressible two-phase flow in porous media, Adv. Water Resour. 85 (2015) 64–78, https://doi.org/10.1016/j.advwatres.2015.09.006.
[53] A. Zidane, A. Firoozabadi, Fracture-cross-flow equilibrium in compositional two-phase reservoir simulation, SPE J. 03 (22) (2017) 0950, https://doi.org/10.2118/184402-PA.
[54] A. Zidane, A. Firoozabadi, Reservoir simulation of fractured media in compressible single-phase multicomponent in 2D, 2.5D and 3D unstructured gridding, Adv. Water Resour. 121 (2018) 68–96, https://doi.org/10.1016/j.advwatres.2018.08.005.
[55] A. Zidane, A. Firoozabadi, Efficient simulation of two-phase compositional flow in fractured reservoirs using 3D unstructured gridding in complex geometries, in: SPE Annual Technical Conference and Exhibition, 2018.
[56] A. Zidane, A. Younes, P. Huggenberger, E. Zechner, The Henry semi-analytical solution for saltwater intrusion with reduced dispersion, Water Resour. Res. 48 (2012) 1–10, https://doi.org/10.1029/2011WR011157.
[57] A. Zidane, E. Zechner, P. Huggenberger, A. Younes, On the effects of subsurface parameters on evaporite dissolution (Switzerland), J. Contam. Hydrol. 160 (2014) 42–52, https://doi.org/10.1016/j.jconhyd.2014.02.006.
[58] A. Zidane, E. Zechner, P. Huggenberger, A. Younes, Simulation of rock salt dissolution and its impact on land subsidence, Hydrol. Earth Syst. Sci. 18 (2014) 2177–2189, https://doi.org/10.5194/hess-18-2177-2014.
[59] O.C. Zienkiewicz, R.L. Taylor, The Finite Element Method, 5th ed., Butterworth-Heinemann, 2000.